


**All-optical magnetization control in CrI<sub>3</sub> monolayers: A microscopic theory**A. Kudlis,<sup>1,\*</sup> M. Kazemi,<sup>2,†</sup> Y. Zhumagulov<sup>Ⓜ,3,‡</sup> H. Schrautzer<sup>Ⓜ,2,§</sup> A. I. Chernov,<sup>4,5,||</sup> P. F. Bessarab<sup>Ⓜ,2,6,¶</sup>  
I. V. Iorsh,<sup>1,\*\*</sup> and I. A. Shelykh<sup>2,1,††</sup><sup>1</sup>*Abrikosov Center for Theoretical Physics, MIPT, Dolgoprudny, Moscow Region 141701, Russia*<sup>2</sup>*Science Institute, University of Iceland, Dunhagi-3, IS-107 Reykjavik, Iceland*<sup>3</sup>*University of Regensburg, Regensburg 93040, Germany*<sup>4</sup>*Russian Quantum Center, Skolkovo, Moscow 143025, Russia*<sup>5</sup>*Center for Photonics and 2D Materials, Moscow Institute of Physics and Technology (National Research University),  
Dolgoprudny 141700, Russia*<sup>6</sup>*Department of Physics and Electrical Engineering, Linnaeus University, SE-39231 Kalmar, Sweden* (Received 1 May 2023; revised 24 August 2023; accepted 25 August 2023; published 13 September 2023)

Bright excitons in ferromagnetic monolayers of CrI<sub>3</sub> efficiently interact with lattice magnetization, which makes all-optical resonant magnetization control possible in this material. Using the combination of *ab initio* simulations within the Bethe-Salpeter approach, semiconductor Bloch equations, and Landau-Lifshitz equations, we construct a microscopic theory of this effect. By solving numerically the resulting set of coupled equations describing the dynamics of atomic spins and spins of the excitons, we demonstrate the possibility of tunable control of the macroscopic magnetization of a sample.

DOI: [10.1103/PhysRevB.108.094421](https://doi.org/10.1103/PhysRevB.108.094421)**I. INTRODUCTION**

Efficient control of the properties of layered structures is an important problem in both fundamental and applied research. In particular, a great demand exists for the development of optimal methods for control of magnetic characteristics of materials. This is not surprising, given the ever-increasing requirements for data-recording capacities of magnetic memory elements. The most important of these are compactness, energy efficiency, and recording speed. Regarding the latter, all-optical methods for magnetic order manipulation look very promising compared with traditional approaches based on the application of an external magnetic field, as device operating frequencies can be enhanced by several orders of magnitude.

To date, there already exist a number of theoretical [1,2] and experimental works confirming the possibility of all-optical magnetization switching (AOMS) in a variety of magnetic compounds, including GdFeCo [3–7] and TbFeCo

[8] ferrimagnetic alloys, as well as in Pt/Co or Co/Gd multilayers [9,10].

Among all candidates where such a reorientation of magnetization is possible, materials combining ferromagnetic ordering with the presence of robust bright excitons are of particular interest [11]. Examples of such materials include chromium trihalides, such as CrCl<sub>3</sub>, CrBr<sub>3</sub>, and CrI<sub>3</sub> [12]. In this paper, we take CrI<sub>3</sub> as an example, but the reported results should remain qualitatively the same for other members of this family. In the material we consider, the Cr<sup>3+</sup> ions are arranged on the honeycomb lattice vertices surrounded by nonmagnetic I<sup>−</sup> ions [13]. Being a two-dimensional (2D) Ising ferromagnet, this material demonstrates a robust optical excitonic response, with record high values of excitonic binding energies and oscillator strengths [14], exceeding even the values reported for transition metal dichalcogenides [15–18].

The combination of such unique properties allowed some of us to propose that chromium trihalides are suitable candidates for polarization-sensitive resonant optical magnetization switching [19], which was later on confirmed experimentally [11]. The process of magnetic reorientation is connected with the transfer of angular momentum from excitons (electron-hole pairs) to the quasilocated *d* electrons of the Cr atoms, and the corresponding phenomenological theory was developed in Ref. [19]. However, the full microscopic theory of the effect is still absent.

In this paper, we make an attempt to construct such a microscopic theory. We apply the well-established atomistic spin dynamics (ASD) formalism as the basis of our work and couple it with the equations for the exciton dynamics by adding the terms describing the interaction between the spins of the excitons and the magnetic lattice. Numerically solving the resulting set of equations allows us to analyze in detail the dynamics of the magnetization switching in real space and time.

\*kudlis.a@mipt.ru

†mak99@hi.is

‡yaruslav.zhumagulov@gmail.com

§hes93@hi.is

||a.chernov@rqc.ru

¶pavel.bessarab@lnu.se

\*\*i.iorsh@metalab.ifmo.ru

††shelykh@hi.is

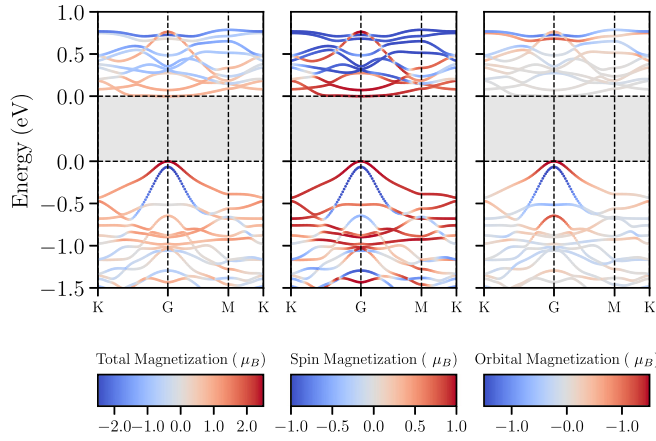


FIG. 1. DFT band structure of excitons in a CrI<sub>3</sub> monolayer with lattice constant 6.69 Å. The color code shows the total, spin, and orbital magnetization in the left, middle, and right panels, respectively. The band-gap energy  $E = 2.59$  eV is indicated by gray shading. According to the first Brillouin zone grid, we have selected 16 valence bands and 14 conduction bands for the exciton basis.

The paper is organized as follows. In Sec. II we present calculations of the excitonic parameters in CrI<sub>3</sub>, and then we present the model Hamiltonian for coupled systems of excitons and lattice spins in Sec. III. Section IV presents the dynamic equations, and Sec. V contains the main results of the work, including the dependence of the switching properties on the parameters of the incident light beam. Section VI summarizes the results of the work.

## II. CALCULATIONS OF EXCITON PARAMETERS FOR CrI<sub>3</sub>

We investigate the electronic structure of ferromagnetic CrI<sub>3</sub> monolayers via first-principles calculations employing density functional theory (DFT). The computations were executed using the GPAW package [20,21]. We use a cut-off energy of 600 eV for the plane-wave basis set and the local-density approximation (LDA) exchange-correlation functional incorporating spin-orbit effects [22]. To mitigate interaction between periodic images, a 16-Å vacuum was used in the supercell.

The lattice constant for the CrI<sub>3</sub> ferromagnetic monolayer was determined via crystal lattice relaxation procedures, resulting in a value of 6.69 Å. The force convergence criteria were set at 1 meV/Å per atom. To address the DFT band-gap issue, a scissor operator was employed to adjust the band-gap value to the experimental value of 2.59 eV [14].

The exciton spectrum was acquired utilizing the GPAW implementation of the Bethe-Salpeter equation [23–26]. Screened Coulomb potential expressions were derived with the dielectric cutoff of 50 eV, 200 electronic bands, and a 2D truncated Coulomb potential [25]. The exciton basis was configured with 16 valence bands and 14 conduction bands on a  $6 \times 6$  grid of the first Brillouin zone.

In Fig. 1, we demonstrate the band structure of the CrI<sub>3</sub> monolayer with color bars for the total, spin, and orbital magnetization which are shown below each panel. The band gap of 2.59 eV is highlighted by the gray area. The analysis

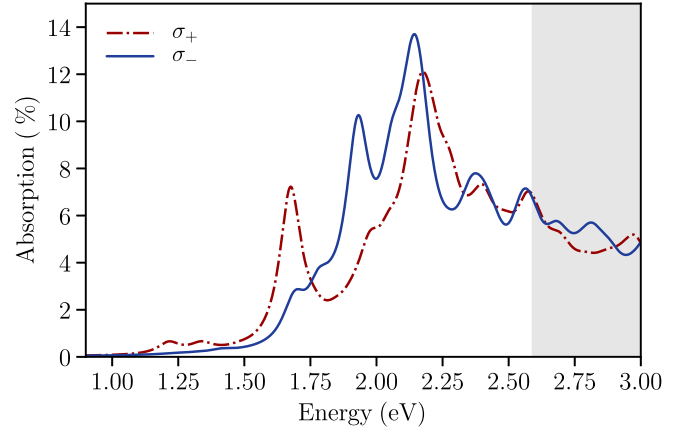


FIG. 2. Absorption spectrum of a CrI<sub>3</sub> sample for two circular polarizations. The solid line and the dash-dotted line correspond to the  $\sigma_-$  and  $\sigma_+$  polarizations, respectively. The band-gap energy  $E = 2.59$  eV is indicated by gray shading.

of the polarization-resolved absorption spectrum of the CrI<sub>3</sub> monolayer is shown in Fig. 2. As one can see, there is a remarkable difference in the absorption of the  $\sigma_+$  and  $\sigma_-$  components. The prominent absorption peaks in both absorption profiles are related to the excitonic transitions. Naturally, if the magnetization of the sample is inverted, the absorption curves corresponding to opposite polarizations interchange. This forms the basis of the magnetization switching mechanism: For a given pump frequency and polarization, the magnetic sublattice tends to orient its magnetization so as to maximize the absorption [19].

## III. THE MODEL HAMILTONIAN

The total energy  $E$  of the system includes three terms,

$$E = E_m + E_{\text{exc}} + E_s, \quad (1)$$

describing the contributions from the magnetic subsystem, the excitonic subsystem, and the interaction between them. The magnetic structure of the CrI<sub>3</sub> monolayer is described within the model of classical spin vectors localized on sites of the honeycomb lattice of the Cr atoms. The corresponding energy is given by

$$E_m = -J \sum_{\langle i,j \rangle} \mathbf{m}_i \cdot \mathbf{m}_j - D \sum_{\langle i,j \rangle} \mathbf{d}_{ij} \cdot [\mathbf{m}_i \times \mathbf{m}_j] - K \sum_i (\mathbf{m}_i \cdot \mathbf{e}_z)^2 - \mu \sum_i \mathbf{B} \cdot \mathbf{m}_i. \quad (2)$$

Here, the first, second, third, and fourth terms describe the Heisenberg exchange, the Dzyaloshinskii-Moriya interaction (DMI), the uniaxial magnetocrystalline anisotropy, and the Zeeman interaction, respectively;  $\mathbf{m}_i$  is the unit vector pointing along the  $i$ th magnetic moment, whose magnitude is  $\mu$  for each lattice site;  $\mathbf{B}$  is the external magnetic field; and  $\mathbf{d}_{ij} = \mathbf{r}_{ij} \times \mathbf{e}_z / |\mathbf{r}_{ij}|$  is the DMI unit vector with  $\mathbf{e}_z$  and  $\mathbf{r}_{ij}$  being the unit vector along the monolayer normal and the vector pointing from site  $i$  to site  $j$ , respectively. The angular brackets indicate summation over unique nearest neighbors only. The effective parameter values are taken from Ref. [27]:  $J = 2.53$  meV,  $D = 1.2$  meV,  $K = 0.153$  meV, and  $\mu = 3.0 \mu_B$ .

The external magnetic field is in the monolayer plane, with the magnitude ranging from 0 to 3.5 T. In our calculations, we use the computational domain of  $N_c = 30 \times 30 = 900$  unit cells equipped with periodic boundary conditions. Note that the number of magnetic moments  $N_a$  explicitly included in the calculations is twice as large as  $N_c$ . The parameters of the magnetic subsystem ensure that parallel alignment of the magnetic moments in the system is a stable magnetic configuration. Uniform magnetization across the computational domain that we use ( $\sim 30$  nm) is consistent with experimental results showing magnetic domain formation in CrI<sub>3</sub> on larger length scales; see, e.g., Refs. [11,28,29].

The Hamiltonian describing the excitonic subsystem reads

$$H_{\text{exc}} = \sum_{\mathbf{q}n} E_{n\mathbf{q}} \hat{X}_{n\mathbf{q}}^\dagger \hat{X}_{n\mathbf{q}} + \mathbf{E}_\pm \sum_n \mathbf{D}_{n\mathbf{q}=0} \hat{X}_{0\mathbf{q}=0}^\dagger \hat{X}_{n\mathbf{k}=0} + \text{H.c.} \quad (3)$$

Here,  $\hat{X}_{n\mathbf{q}}^\dagger$  ( $\hat{X}_{n\mathbf{q}}$ ) is the exciton creation (annihilation) operator characterized by momentum  $\mathbf{q}$  and band index  $n$ ;  $E_{n\mathbf{q}}$  is the exciton energy;  $\mathbf{D}_{n\mathbf{q}=0}$  is the dipole moment of the optical transition obtained from the DFT calculations (see Appendix A), here limited to the direct-gap transitions; and  $\mathbf{E}_\pm(t) = \text{Re}[(E_0, \mp iE_0, 0) \exp(-i\omega t)]h(t)$  is the right- or left-circularly polarized electric field characterized by the pulse envelope  $h(t)$ . The effects of both radiative and nonradiative damping are described phenomenologically; see Appendix B for details.

The interaction between the excitonic and magnetic subsystems is characterized by the following Hamiltonian:

$$H_s = -g\mu \sum_{\mathbf{q}\mathbf{q}'m'} (\mathbf{m}_{\mathbf{q}-\mathbf{q}'} - \mathbf{m}_{\mathbf{q}-\mathbf{q}'}) \mathbf{M}_{nn'}^{\mathbf{q}\mathbf{q}'} \hat{X}_{n\mathbf{q}}^\dagger \hat{X}_{n'\mathbf{q}'}, \quad (4)$$

where the term inside the parentheses is the Fourier transform of the magnetization relative to the collinear ground state (see Appendix C),  $\mathbf{M}_{nn'}^{\mathbf{q}\mathbf{q}'}$  is the dipole matrix element describing the interaction with the local magnetic moment, and  $g$  is the on-site spin-exciton coupling constant (see Appendix A for details). The evaluation of the coupling constant  $g$  cannot be performed using standard DFT approaches and requires a separate consideration which goes beyond the scope of this paper. Here,  $g$  is taken as a phenomenological parameter with the value  $g = 2.3$  meV, which is slightly less than the exchange interaction parameter in the magnetic lattice Hamiltonian.

Note that exciton-exciton interaction is neglected and only the single-exciton wave function  $\Psi_{\text{exc}}$  is considered explicitly. Therefore

$$E_s \approx n_{\text{exc}} \langle \Psi_{\text{exc}} | H_s | \Psi_{\text{exc}} \rangle = -g\mu \sum_i \sigma_i (\mathbf{m}_i - \mathbf{m}_i^g). \quad (5)$$

Here,  $n_{\text{exc}}$  is the scaling factor proportional to the number of unit cells (in our case,  $n_{\text{exc}} = 450$ ),  $\mathbf{m}_i^g \equiv \mathbf{e}_z$  is the unit vector along the ground-state magnetization, and  $\sigma_i$  is the exciton spin vector associated with the  $i$ th unit cell (note that excitons in CrI<sub>3</sub> are of the Frenkel type) defined via the equation

$$\sigma_i = n_{\text{exc}} \sum_{\mathbf{q}\mathbf{q}'} e^{2\pi i(\mathbf{r}_i(\mathbf{q}'-\mathbf{q}))N_c} \sum_{nn'} C_n^{\mathbf{q}\mathbf{q}'} \mathbf{M}_{nn'}^{\mathbf{q}\mathbf{q}'} C_{n'}^{\mathbf{q}}, \quad (6)$$

where  $\mathbf{r}_i$  is the position of  $i$ th unit cell and  $C_n^{\mathbf{q}}$  are the expansion coefficients of  $\Psi_{\text{exc}}$ :

$$\Psi_{\text{exc}} = \sum_{n\mathbf{q}} C_n^{\mathbf{q}} \hat{X}_{n\mathbf{q}}^\dagger |0\rangle. \quad (7)$$

#### IV. DYNAMIC EQUATIONS

The dynamic equations for the observables follow from the model Hamiltonian. The evolution of  $\Psi_{\text{exc}}$  is accessed via the equation of motion for its coefficients:

$$i\hbar \frac{\partial C_n^{\mathbf{q}}}{\partial t} = \sum_{n'\mathbf{q}'} H_{nn'}^{\mathbf{q}\mathbf{q}'}(t) C_{n'}^{\mathbf{q}'}(t), \quad (8)$$

where  $H_{nn'}^{\mathbf{q}\mathbf{q}'}$  are the matrix elements of the excitonic Hamiltonian  $H = H_{\text{exc}} + H_s$ . On the other hand, the dynamics of the lattice magnetization is obtained via the time integration of the Landau-Lifshitz-Gilbert equation (LLGE) for the normalized magnetization vectors at zero temperature:

$$\frac{d\mathbf{m}_i}{dt} = -\gamma \mathbf{m}_i \times \mathbf{B}_i^{\text{eff}} + \eta \left( \mathbf{m}_i \times \frac{d\mathbf{m}_i}{dt} \right), \quad (9)$$

where  $\gamma$  is the gyromagnetic ratio,  $\eta$  is the dimensionless damping parameter (in this paper we take  $\eta = 0.1, 0.2$ ), and  $\mathbf{B}_i^{\text{eff}}$  is the effective magnetic field defined as

$$\mathbf{B}_i^{\text{eff}} = -\frac{1}{\mu} \frac{\partial E}{\partial \mathbf{m}_i} = g\sigma_i - \frac{1}{\mu} \frac{\partial E_m}{\partial \mathbf{m}_i}, \quad (10)$$

where use was made of Eq. (5) and the fact that only  $E_s + E_m$  depends explicitly on  $\mathbf{m}_i$ . Note that the effect of excitons on the magnetization dynamics is treated within the mean-field approach, where the magnetization-exciton interaction energy  $E_s$  depends on the exciton spin vector configuration  $\sigma$  [see Eq. (5)], which needs to be updated every time step using (8) and (6). We use the semi-implicit solver by Mentink *et al.* [30] for the time integration of the LLGE. We do not include thermal fluctuations in our simulations so as to focus on exciton dynamics as the main driving force of the magnetization switching [11].

#### V. RESULTS AND DISCUSSION

We study the dynamics of the system induced by a spatially homogeneous circularly polarized laser pulse at normal incidence. The choice of the pulse envelope  $h(t)$  is inspired by real setups [11,29]:

$$h(t) = A\theta(t_f - |2t - t_f|) \exp \left[ -B \left( \frac{t - t_f/2}{t_f} \right)^2 \right]. \quad (11)$$

Here,  $t_f$  is the duration of the pulse, and  $A = 1.94$  and  $B = 32.2$  are dimensionless parameters defining the total pulse fluence  $F$ :

$$F = \frac{E_0^2 c \epsilon_0}{2} \int_0^{t_f} h(t)^2 dt = C I_0 t_f, \quad (12)$$

where  $I_0 = E_0^2 c \epsilon_0$  is the intensity of the pulse and  $C = A^2 \text{erf}(\sqrt{B}/2) \sqrt{\pi}/(2B)$  is the dimensionless constant. In our calculations, the intensity never exceeds the value of 0.1 TW/cm<sup>2</sup>, which is consistent with experiments [11,29]. We



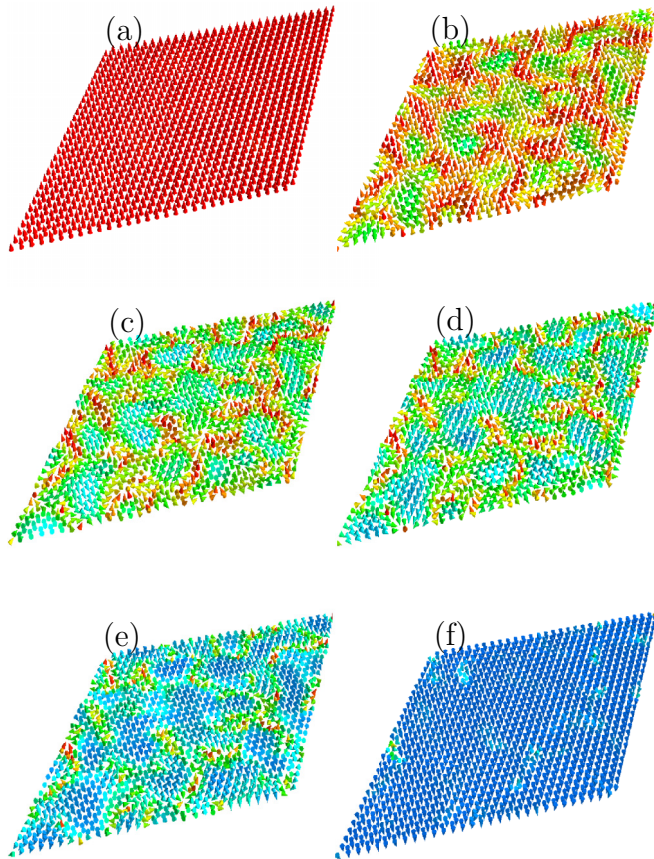


FIG. 3. Evolution of the magnetic structure of the system for the pulse fluence  $F_1 = 166 \text{ mJ/cm}^2$ . The fluence magnitude is sufficient to induce the magnetization reversal. The snapshots [(a)–(f)] correspond to 1.6, 1.8, 1.84, 1.86, 1.9, and 2.04 ps, respectively. The color codes the orientation of the magnetic moments of the Cr atoms. This case corresponds to the solid line in Fig. 5.

take the duration of the pulse  $t_f = 4 \text{ ps}$  and its central frequency  $\omega = 1.94 \text{ eV}$ , which is below the direct band gap. Note that the chosen value of  $\omega$  is in the vicinity of one of the  $\sigma^-$  peaks in the absorption spectrum.

The initial magnetization direction is prepared by aligning all magnetic vectors along  $e_z$  and perturbing them with a small amount of random noise to break the symmetry. The simulation of the spatiotemporal magnetization pattern provides information about the evolution of the cumulative out-of-plane magnetization due to the spin lattice and excitons:

$$M_z^m(t) = \frac{1}{N_a} \sum_{i=1}^{N_a} m_i^z(t), \quad M_z^\sigma(t) = \frac{1}{N_c} \sum_{i=1}^{N_c} \sigma_i^z(t). \quad (13)$$

The dynamics of the magnetization switching is shown in Fig. 3. The arrival of the pulse with  $\sigma^-$  polarization leads to the appearance of the domains with inverted magnetization. The domains are distributed randomly due to noise in the initial conditions for the magnetization. If the fluence exceeds some critical value  $F_c$ , the size of the domains increases with time, making the system eventually reach the state with spatially homogeneous inverted magnetization (see Fig. 3). On the other hand, if the fluence is below the critical value, the growth of the domains with opposite magnetization is not

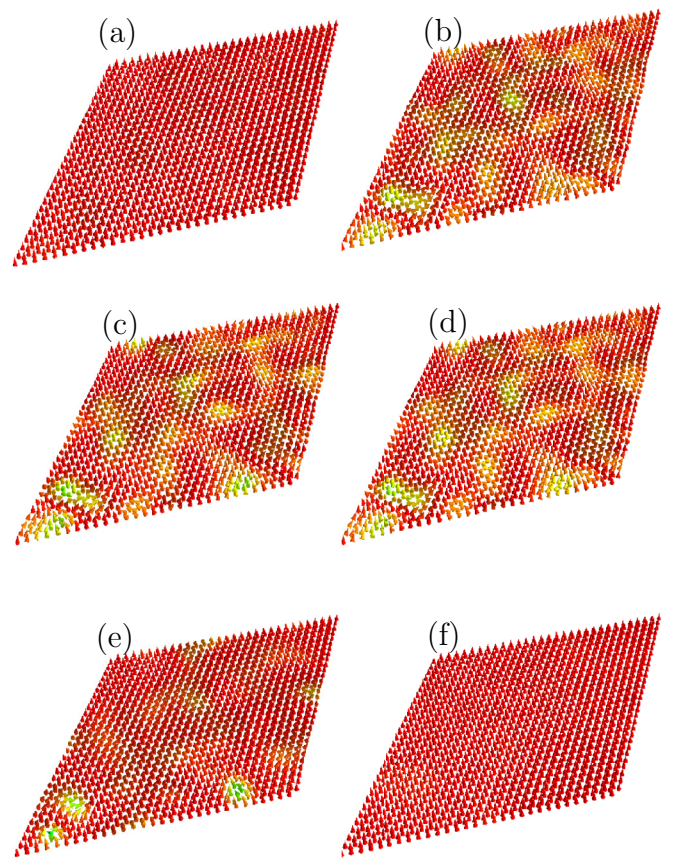


FIG. 4. Evolution of the magnetic structure of the system for the pulse fluence  $F_2 = 33 \text{ mJ/cm}^2$ . The fluence magnitude is insufficient to induce the magnetization reversal. The snapshots [(a)–(f)] correspond to 2.2, 2.76, 2.98, 3.2, 4.4, and 8.0 ps, respectively. The color codes the orientation of the magnetic moments of the Cr atoms. This case corresponds to the dashed line in Fig. 5.

sufficient for the reversal, and the system relaxes back to the initial homogeneous state (see Fig. 4).

The dynamics of the cumulative magnetization is shown in Fig. 5. The transition between up and down polarized states induced by the pulse is quite abrupt, which makes it possible to introduce the characteristic switching time  $\tau$ —the principal parameter characterizing the magnetization reversal. As expected,  $\tau$  decreases with increasing  $F$  (see Fig. 6). The switching time becomes infinite when the fluence reaches the critical value  $F_c \approx 46 \text{ mJ/cm}^2$ , below which no magnetization reversal is possible. This behavior agrees well with our previous study based on the phenomenological model of resonant magnetization switching [19]. We point out, however, that the details of switching depend on the parameters of the microscopic Hamiltonian as well as on the shape of the pump pulse. Ultimately, magnetization switching is realized if the system overcomes the energy barrier produced by the magnetic anisotropy. Additionally, the critical fluence and the switching time are affected by the exciton decay rate  $\delta$  (see Appendix B) and the damping parameter  $\eta$ . For example, for a fixed pulse fluence of  $166 \text{ mJ/cm}^2$ , the switching time increases from 1.85 to 2.07 ps when the damping factor  $\eta$  decreases from 0.2 to 0.1 (see Fig. 5). Interestingly, the switching time is also

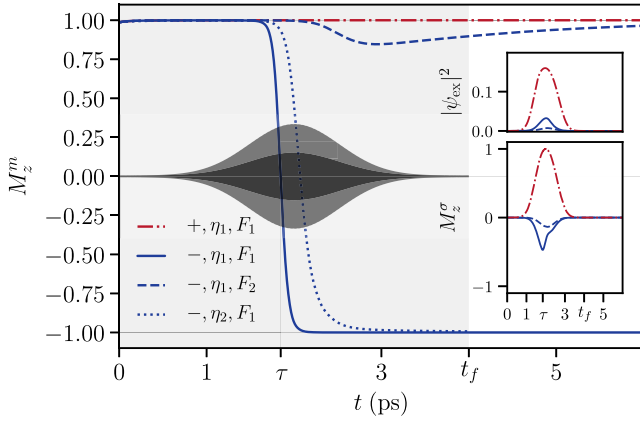


FIG. 5. Time dependence of the cumulative out-of-plane magnetization  $M_z^m$  for different light polarizations. The blue shaded area indicates the laser pulse duration. The upper inset shows the time dependence of  $|\psi_{\text{ex}}|^2 = |\Psi_{\text{exc}}|^2 - |\psi_0|^2$  describing the evolution of excited exciton states. The lower inset shows the time dependence of the exciton magnetization. Gray areas show the envelope functions for the optical pump pulse with fluence  $F_1 = 166 \text{ mJ/cm}^2$  (lighter gray, magnetization reversal occurs) and  $F_2 = 33.2 \text{ mJ/cm}^2$  (darker gray, magnetization reversal does not occur). The switching time  $\tau$  is defined by the instant when  $M_z^m$  changes sign. Here,  $\tau = 1.85 \text{ ps}$ . The signs  $+$  and  $-$  correspond to right-hand and left-hand circularly polarized light, respectively.

influenced by the lateral magnetic field  $B$  (see inset in Fig. 6). For the considered lateral field range and a pulse fluence of  $133 \text{ mJ/cm}^2$ ,  $\tau$  decreases linearly with increasing  $B$ .

While the dynamics of the excitons affects the magnetization of the system, the opposite is also valid. In particular, ferromagnetic coupling between the subsystems leads to more productive excitation of excitons whose effective magnetization is along the lattice magnetization, as illustrated in the insets of Fig. 5.

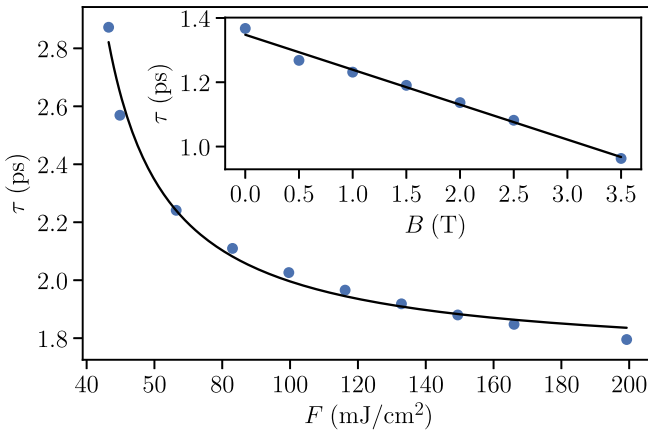


FIG. 6. Magnetization switching time  $\tau$  as a function of pump fluence  $F$ . Magnetization switching is achieved if the fluence of the pulse exceeds a critical value  $F_c \approx 46 \text{ mJ/cm}^2$ , at which the switching time diverges. The inset shows the switching time as a function of the lateral external magnetic field for a fluence of  $133 \text{ mJ/cm}^2$ .

A change in the circular polarization of the incident beam modifies drastically the magnetization dynamics: The switching does not occur for the initial magnetization pointing up, but can happen for the initial magnetization pointing down.

## VI. CONCLUSION

In conclusion, we developed a microscopic theory of all-optical resonant polarization-sensitive magnetization switching in monolayers of CrI<sub>3</sub>. The effect is due to the combination of the peculiar optical selection rules for excitons in this material and efficient coupling of excitons to the magnetic lattice. The spatiotemporal distribution of the magnetization under circularly polarized pulses was investigated, and the dependence of the parameters characterizing the switching on the properties of the optical pulse was determined.

The exciton-mediated magnetization switching was obtained here without including thermal fluctuations in the simulations. It remains to be seen how thermal effects influence the coupled exciton-magnetization dynamics and, in particular, whether thermal fluctuations can assist magnetization switching. This is a subject for future research.

## ACKNOWLEDGMENTS

A.K., M.K., and I.A.S. acknowledge support from the Icelandic Research Fund (Grant No. 163082-051). P.F.B. acknowledges support from the Icelandic Research Fund (Grant No. 217750), the University of Iceland Research Fund (Grant No. 15673), and the Swedish Research Council (Grant No. 2020-05110). A.K. thanks the University of Iceland for hospitality during the work on the current project. I.V.I. and I.A.S. acknowledge support from a joint RFBR-DFG project, Project No. 21-52-12038. The work of A.I.C. and I.V.I. was supported by Rosatom in the framework of the Roadmap for Quantum Computing (Contract No. 868-1.3-15/15-2021 dated October 5). Y.Z. is grateful to Deutsche Forschungsgemeinschaft (DFG, German Research Foundation) SPP 2244 (Project No. 443416183) for financial support.

## APPENDIX A: MATRIX ELEMENTS OF THE EXCITON HAMILTONIAN

The matrix elements of the exciton Hamiltonian  $H_{\text{exc}} + H_s$  are computed via the resolution of the Bethe-Salpeter equation (BSE) parametrized using the first-principles calculations. The exciton wave functions and associated energies are obtained by diagonalizing the BSE Hamiltonian [23,31,32] as follows:

$$\sum_{c'v'k'} H_{cvkc'v'k'}^{\text{BSE}}(\mathbf{q}) A_{c'v'k'}^{n\mathbf{q}} = E^{n\mathbf{q}} A_{cv\mathbf{q}}^{n\mathbf{q}}. \quad (\text{A1})$$

Here,  $H_{cvkc'v'k'}^{\text{BSE}}(\mathbf{q})$  are the matrix elements of the BSE Hamiltonian for excitons possessing momentum  $\mathbf{q}$ , and  $A_{cv\mathbf{q}}^{n\mathbf{q}}$  and  $E^{n\mathbf{q}}$  are the  $n$ th exciton wave function and energy, respectively. The indices  $c$  ( $c'$ ),  $v$  ( $v'$ ), and  $\mathbf{k}$  ( $\mathbf{k}'$ ) denote the conduction band, valence band, and single-particle momentum, respectively. The Hamiltonian  $H^{\text{BSE}}$  is calculated using the Tamm-Dancoff approximation [31], which is particularly well suited for wide-gap semiconductors. This approximation

disregards the coupling between resonance and antiresonance poles while preserving the Hermitian character of the Hamiltonian.

The calculation of the dipole matrix elements is carried out utilizing the following equation:

$$\mathbf{D}_{n\mathbf{q}=0} = \langle 0|\mathbf{r}|n\mathbf{q} = 0\rangle = \sum_{c\nu\mathbf{k}} A_{c\nu\mathbf{k}}^{n\mathbf{q}=0} \langle \nu\mathbf{k}|\mathbf{r}|c\mathbf{k}\rangle, \quad (\text{A2})$$

where  $\langle \nu\mathbf{k}|\mathbf{r}|c\mathbf{k}\rangle$  is the single-particle dipole matrix element corresponding to the optical transition from the conduction band  $c$  to the valence band  $\nu$  with momentum  $\mathbf{k}$ .

The key ingredients of the exciton-skyrmion Hamiltonian interaction are the matrix elements of the exciton magnetic moment  $\mathbf{M}_{nn'}^{\mathbf{q}\mathbf{q}'}$ . These matrix elements are assembled from the matrix elements of the spin magnetic moment  $\mathbf{S}_{nn'}^{\mathbf{q}\mathbf{q}'}$  and the orbital magnetic moment  $\mathbf{L}_{nn'}^{\mathbf{q}\mathbf{q}'}$ . The matrix elements of the spin magnetic moment are calculated from the single-particle spin moment:

$$\begin{aligned} \mathbf{S}_{nn'}^{\mathbf{q}\mathbf{q}'} &= \sum_{c\nu\mathbf{k}, c'\nu'\mathbf{k}'} (A_{c\nu\mathbf{k}}^{n\mathbf{q}})^* A_{c'\nu'\mathbf{k}'}^{n'\mathbf{q}'} \\ &\times [\langle c\mathbf{k} + \mathbf{q}|\mathbf{S}|c'\mathbf{k}' + \mathbf{q}'\rangle - \langle \nu'\mathbf{k}'|\mathbf{S}|\nu\mathbf{k}\rangle], \end{aligned} \quad (\text{A3})$$

where  $\langle c\mathbf{k}|\mathbf{S}|c'\mathbf{k}'\rangle$  is the single-particle spin matrix element. While the single-particle spin operators are simply defined using the Pauli matrices in the spin subspace, the calculation of the orbital moment requires a more careful consideration. In this paper, we employ a local projector augmented wave (PAW) technique to evaluate the orbital single-particle magnetic moment, as it offers a more straightforward approach compared with the previously reported perturbation-theory-based methods [33–37]. All-electron orbitals inside the PAW sphere can be expanded as [20,38]

$$|c\mathbf{k}\rangle = \sum_i \langle p_i^a | \varphi_{c\mathbf{k}} \rangle | \phi_i^a \rangle, \quad (\text{A4})$$

where  $p_i^a$  is a projector of the smooth pseudo wave function  $\varphi_{c\mathbf{k}}$  for band  $c$  with momentum  $\mathbf{k}$  on the  $i$ th all-electron partial wave for atom  $a$ ,  $\phi_i^a$ . We calculate the one-particle matrix elements of the orbital momentum as follows [22]:

$$\langle c\mathbf{k}|\mathbf{L}|c'\mathbf{k}'\rangle = \sum_{ai_1i_2} \langle \varphi_{c\mathbf{k}} | p_{i_1}^a \rangle \langle \phi_{i_1}^a | \mathbf{L}^a | \phi_{i_2}^a \rangle \langle p_{i_2}^a | \varphi_{c'\mathbf{k}'} \rangle, \quad (\text{A5})$$

where  $\mathbf{L}^a$  is the orbital momentum operator for atom  $a$ . Since partial waves  $\phi_i^a$  are usually defined in a spherical basis, the matrix elements  $\langle \phi_{i_1}^a | \mathbf{L}^a | \phi_{i_2}^a \rangle$  can be calculated analytically. Having single-particle matrix elements of the orbital magnetic moment, we compute the exciton matrix elements as follows:

$$\begin{aligned} \mathbf{L}_{nn'}^{\mathbf{q}\mathbf{q}'} &= \sum_{c\nu\mathbf{k}, c'\nu'\mathbf{k}'} (A_{c\nu\mathbf{k}}^{n\mathbf{q}})^* A_{c'\nu'\mathbf{k}'}^{n'\mathbf{q}'} \\ &\times [\langle c\mathbf{k} + \mathbf{q}|\mathbf{L}|c'\mathbf{k}' + \mathbf{q}'\rangle - \langle \nu'\mathbf{k}'|\mathbf{L}|\nu\mathbf{k}\rangle]. \end{aligned} \quad (\text{A6})$$

The total exciton magnetic moment is obtained by computing a sum of the spin and orbital components:

$$\mathbf{M}_{nn'}^{\mathbf{q}\mathbf{q}'} = \mathbf{L}_{nn'}^{\mathbf{q}\mathbf{q}'} + \mathbf{S}_{nn'}^{\mathbf{q}\mathbf{q}'}. \quad (\text{A7})$$

## APPENDIX B: INTRODUCTION OF DAMPING

The effects of damping are modeled by introducing finite inverse relaxation time  $\delta$ , which results in the decay of excited excitonic states  $\sim \exp(-\Delta t \delta)$  with time  $\Delta t$ . Since we do not have data for the exciton-state-resolved damping, we assume, for simplicity, the same damping parameter for all excited excitonic states. Note that an increase in the damping parameter leads to an increase in the switching time. Therefore, at each time step of the simulation, the vector of state  $\Psi_{\text{exc}} = (\psi_0, \psi_1, \dots, \psi_n)$ , with  $\psi_0$  being the component responsible for the vacuum, is substituted by the modified vector of state  $\Psi_{\text{exc}} \leftarrow \tilde{\Psi}_{\text{exc}} = (\tilde{\psi}_0, \tilde{\psi}_1, \dots, \tilde{\psi}_n)$ , whose components are defined via the following operations:

$$\tilde{\psi}_i = \psi_i \sqrt{1 - \Delta t \delta}, \quad i > 0, \quad (\text{B1})$$

$$\Delta = 1 - \left( \sum_{i=1}^n |\tilde{\psi}_i|^2 + |\psi_0|^2 \right), \quad (\text{B2})$$

$$\tilde{\psi}_0 = \psi_0 \frac{\sqrt{\Delta + |\psi_0|^2}}{|\psi_0|}. \quad (\text{B3})$$

Note that  $|\tilde{\Psi}_{\text{exc}}| = |\Psi_{\text{exc}}| = 1$ . In this paper, we take  $\delta = 80$  meV based on the previously calculated exciton absorption line broadening [14].

## APPENDIX C: FOURIER TRANSFORMS

The definition of the direct and inverse Fourier transforms used in this paper requires a special discussion since the gratings in the real space  $r$  and momentum space  $q$  have different discreteness. For an arbitrary function  $f$ , the Fourier transforms are defined via the following equations:

$$f(\mathbf{r}_i) = \sum_j^{N_q} \exp[2\pi i(\mathbf{r}_i \mathbf{q}_j)_{N_c}] f(\mathbf{q}_j), \quad (\text{C1})$$

$$f(\mathbf{q}_j) = \frac{1}{N_c} \sum_i^{N_c} \exp[-2\pi i(\mathbf{r}_i \mathbf{q}_j)_{N_c}] f(\mathbf{r}_i), \quad (\text{C2})$$

where  $N_c = 30 \times 30 = 900$  is the number of unit cells and  $N_q = 6 \times 6 = 36$  is the number of points in the  $q$  space. We define the dot product  $(\cdot)_{N_c}$  as

$$(\mathbf{r}\mathbf{q})_{N_c} = \frac{r_i^x q_j^x}{N_c^x} + \frac{r_i^y q_j^y}{N_c^y} + \frac{r_i^z q_j^z}{N_c^z}. \quad (\text{C3})$$

We use  $N_c^x = N_c^y = 30$  and  $N_c^z = 1$ . Since there are two magnetic atoms per unit cell, we adhere to the following formula to compute the Fourier transform of the magnetization:

$$\begin{aligned} \mathbf{m}_{\mathbf{q}-\mathbf{q}'} &= \frac{1}{N_c} \sum_i^{N_c} \exp[-2\pi i(\mathbf{r}_i(\mathbf{q} - \mathbf{q}'))_{N_c}] \\ &\times (\mathbf{m}_{2i} + \mathbf{m}_{2i-1}), \end{aligned} \quad (\text{C4})$$

where we use the total magnetic moment of the unit cell.



- [1] J. Gorchon, R. B. Wilson, Y. Yang, A. Pattabi, J. Y. Chen, L. He, J. P. Wang, M. Li, and J. Bokor, Role of electron and phonon temperatures in the helicity-independent all-optical switching of GdFeCo, *Phys. Rev. B* **94**, 184406 (2016).
- [2] R. Moreno, T. A. Ostler, R. W. Chantrell, and O. Chubykalo-Fesenko, Conditions for thermally induced all-optical switching in ferrimagnetic alloys: Modeling of TbCo, *Phys. Rev. B* **96**, 014409 (2017).
- [3] D. O. Ignatyeva, C. S. Davies, D. A. Sylgacheva, A. Tsukamoto, H. Yoshikawa, P. O. Kapralov, A. Kirilyuk, V. I. Belotelov, and A. V. Kimel, Plasmonic layer-selective all-optical switching of magnetization with nanometer resolution, *Nat. Commun.* **10**, 4786 (2019).
- [4] L. Aviles-Flix, A. Olivier, G. Li, C. S. Davies, L. Alvaro-Gomez, M. Rubio-Roy, S. Auffret, A. Kirilyuk, A. V. Kimel, Th. Rasing, L. D. Buda-Prejbeanu, R. C. Sousa, B. Dieny, and I. L. Prejbeanu, Single-shot all-optical switching of magnetization in Tb/Co multilayer-based electrodes, *Sci. Rep.* **10**, 5211 (2020).
- [5] C. D. Stanciu, F. Hansteen, A. V. Kimel, A. Kirilyuk, A. Tsukamoto, A. Itoh, and Th. Rasing, All-Optical Magnetic Recording with Circularly Polarized Light, *Phys. Rev. Lett.* **99**, 047601 (2007).
- [6] C. S. Davies, T. Janssen, J. H. Mentink, A. Tsukamoto, A. V. Kimel, A. F. G. van der Meer, A. Stupakiewicz, and A. Kirilyuk, Pathways for Single-Shot All-Optical Switching of Magnetization in Ferrimagnets, *Phys. Rev. Appl.* **13**, 024064 (2020).
- [7] J. Igarashi, Q. Remy, S. Iihama, G. Malinowski, M. Hehn, J. Gorchon, J. Hohlfeld, S. Fukami, H. Ohno, and S. Mangin, Engineering single-shot all-optical switching of ferromagnetic materials, *Nano Lett.* **20**, 8654 (2020).
- [8] X. Lu, X. Zou, D. Hinzke, T. Liu, Y. Wang, T. Cheng, J. Wu, T. A. Ostler, J. Cai, U. Nowak, R. W. Chantrell, Y. Zhai, and Y. Xu, Roles of heating and helicity in ultrafast all-optical magnetization switching in TbFeCo, *Appl. Phys. Lett.* **113**, 032405 (2018).
- [9] M. S. El Hadri, P. Pirro, C.-H. Lambert, S. Petit-Watelot, Y. Quessab, M. Hehn, F. Montaigne, G. Malinowski, and S. Mangin, Two types of all-optical magnetization switching mechanisms using femtosecond laser pulses, *Phys. Rev. B* **94**, 064412 (2016).
- [10] Y. L. W. van Hees, P. van de Meughevel, B. Koopmans, and R. Lavrijsen, Deterministic all-optical magnetization writing facilitated by non-local transfer of spin angular momentum, *Nat. Commun.* **11**, 3835 (2020).
- [11] P. Zhang, T.-F. Chung, Q. Li, S. Wang, Q. Wang, W. L. B. Huey, S. Yang, J. E. Goldberger, J. Yao, and X. Zhang, All-optical switching of magnetization in atomically thin CrI<sub>3</sub>, *Nat. Mater.* **21**, 1373 (2022).
- [12] B. Huang, G. Clark, D. R. Klein, D. MacNeill, E. Navarro-Moratalla, K. L. Seyler, N. Wilson, M. A. McGuire, D. H. Cobden, D. Xiao, W. Yao, P. Jarillo-Herrero, and X. Xu, Electrical control of 2D magnetism in bilayer CrI<sub>3</sub>, *Nat. Nanotechnol.* **13**, 544 (2018).
- [13] M. A. McGuire, H. Dixit, V. R. Cooper, and B. C. Sales, Coupling of crystal structure and magnetism in the layered, ferromagnetic insulator CrI<sub>3</sub>, *Chem. Mater.* **27**, 612 (2015).
- [14] M. Wu, Z. Li, T. Cao, and S. G. Louie, Physical origin of giant excitonic and magneto-optical responses in two-dimensional ferromagnetic insulators, *Nat. Commun.* **10**, 2371 (2019).
- [15] A. Chernikov, T. C. Berkelbach, H. M. Hill, A. Rigosi, Y. Li, B. Aslan, D. R. Reichman, M. S. Hybertsen, and T. F. Heinz, Exciton Binding Energy and Nonhydrogenic Rydberg Series in Monolayer WS<sub>2</sub>, *Phys. Rev. Lett.* **113**, 076802 (2014).
- [16] A. Splendiani, L. Sun, Y. Zhang, T. Li, J. Kim, C.-Y. Chim, G. Galli, and F. Wang, Emerging photoluminescence in monolayer MoS<sub>2</sub>, *Nano Lett.* **10**, 1271 (2010).
- [17] P. Steinleitner, P. Merkl, P. Nagler, J. Mornhinweg, C. Schüller, T. Korn, A. Chernikov, and R. Huber, Direct observation of ultrafast exciton formation in a monolayer of WSe<sub>2</sub>, *Nano Lett.* **17**, 1455 (2017).
- [18] G. Wang, A. Chernikov, M. M. Glazov, T. F. Heinz, X. Marie, T. Amand, and B. Urbaszek, Colloquium: Excitons in atomically thin transition metal dichalcogenides, *Rev. Mod. Phys.* **90**, 021001 (2018).
- [19] A. Kudlis, I. Iorsh, and I. A. Shelykh, All-optical resonant magnetization switching in CrI<sub>3</sub> monolayers, *Phys. Rev. B* **104**, L020412 (2021).
- [20] J. J. Mortensen, L. B. Hansen, and K. W. Jacobsen, Real-space grid implementation of the projector augmented wave method, *Phys. Rev. B* **71**, 035109 (2005).
- [21] J. Enkovaara, C. Rostgaard, J. J. Mortensen, J. Chen, M. Duřak, L. Ferrighi, J. Gavnholt, C. Glinsvad, V. Haikola, H. A. Hansen, H. H. Kristoffersen, M. Kuisma, A. H. Larsen, L. Lehtovaara, M. Ljungberg, O. Lopez-Acevedo, P. G. Moses, J. Ojanen, T. Olsen, V. Petzold *et al.*, Electronic structure calculations with GPAW: A real-space implementation of the projector augmented-wave method, *J. Phys.: Condens. Matter* **22**, 253202 (2010).
- [22] T. Olsen, Designing in-plane heterostructures of quantum spin Hall insulators from first principles: 1T' - MoS<sub>2</sub> with adsorbates, *Phys. Rev. B* **94**, 235106 (2016).
- [23] M. Rohlfing and S. G. Louie, Electron-hole excitations and optical spectra from first principles, *Phys. Rev. B* **62**, 4927 (2000).
- [24] J. Yan, J. J. Mortensen, K. W. Jacobsen, and K. S. Thygesen, Linear density response function in the projector augmented wave method: Applications to solids, surfaces, and interfaces, *Phys. Rev. B* **83**, 245122 (2011).
- [25] F. Hüser, T. Olsen, and K. S. Thygesen, How dielectric screening in two-dimensional crystals affects the convergence of excited-state calculations: Monolayer MoS<sub>2</sub>, *Phys. Rev. B* **88**, 245309 (2013).
- [26] T. Olsen, Unified Treatment of Magnons and Excitons in Monolayer CrI<sub>3</sub> from Many-Body Perturbation Theory, *Phys. Rev. Lett.* **127**, 166402 (2021).
- [27] A. K. Behera, S. Chowdhury, and S. R. Das, Magnetic skyrmions in atomic thin CrI<sub>3</sub> monolayer, *Appl. Phys. Lett.* **114**, 232402 (2019).
- [28] L. Thiel, Z. Wang, M. A. Tschudin, D. Rohner, I. Gutiérrez-Lezama, N. Ubrig, M. Gibertini, E. Giannini, A. F. Morpurgo, and P. Maletinsky, Probing magnetism in 2D materials at the nanoscale with single-spin microscopy, *Science* **364**, 973 (2019).
- [29] M. Dabrowski, S. Guo, M. Strungaru, P. S. Keatley, F. Withers, E. J. G. Santos, and R. J. Hicken, All-optical control of spin in a 2D van der Waals magnet, *Nat. Commun.* **13**, 5976 (2022).

- [30] J. H. Mentink, M. V. Tretyakov, A. Fasolino, M. I. Katsnelson, and T. Rasing, Stable and fast semi-implicit integration of the stochastic Landau–Lifshitz equation, *J. Phys.: Condens. Matter* **22**, 176001 (2010).
- [31] G. Onida, L. Reining, and A. Rubio, Electronic excitations: density-functional versus many-body Green’s-function approaches, *Rev. Mod. Phys.* **74**, 601 (2002).
- [32] M. Rohlfing and S. G. Louie, Electron-Hole Excitations in Semiconductors and Insulators, *Phys. Rev. Lett.* **81**, 2312 (1998).
- [33] T. Deilmann, P. Krüger, and M. Rohlfing, *Ab Initio* Studies of Exciton  $g$  Factors: Monolayer Transition Metal Dichalcogenides in Magnetic Fields, *Phys. Rev. Lett.* **124**, 226402 (2020).
- [34] T. Woźniak, P. E. Faria Junior, G. Seifert, A. Chaves, and J. Kunstmann, Exciton  $g$  factors of van der Waals heterostructures from first-principles calculations, *Phys. Rev. B* **101**, 235408 (2020).
- [35] M. G. Lopez, D. Vanderbilt, T. Thonhauser, and I. Souza, Wannier-based calculation of the orbital magnetization in crystals, *Phys. Rev. B* **85**, 014435 (2012).
- [36] T. Thonhauser, D. Ceresoli, D. Vanderbilt, and R. Resta, Orbital Magnetization in Periodic Insulators, *Phys. Rev. Lett.* **95**, 137205 (2005).
- [37] D. Ceresoli, T. Thonhauser, D. Vanderbilt, and R. Resta, Orbital magnetization in crystalline solids: Multi-band insulators, Chern insulators, and metals, *Phys. Rev. B* **74**, 024408 (2006).
- [38] P. E. Blöchl, Projector augmented-wave method, *Phys. Rev. B* **50**, 17953 (1994).